Supplement of Atmos. Chem. Phys., 26, 8021–8050, 2026
https://doi.org/10.5194/acp-26-8021-2026-supplement

Atmospheric Chemistry and Physics
Open Access

Supplement of

NO_x emissions constraints from GEMS NO_2 retrievals: inversion methodology and air quality model evaluation in Bangkok using ASIA-AQ multi-platform observations

Julianna A. Christopoulos et al.

Correspondence to: Julianna A. Christopoulos (juliechristo@g.ucla.edu)

S1 Supplementary Methods

S1.1 Gaussian Plume (GP) Inversion Method

We apply a Gaussian plume model method to estimate NO_x emissions over Bangkok as outlined in Kuhlmann et al., 2024. This approach fits a vertically integrated Gaussian plume model to GEMS-observed NO_2 column densities, accounting for wind advection, plume dispersion, and chemical loss. The Gaussian plume model for a point source is expressed as:

$$G(x,y) = \frac{QH(x)}{2\sqrt{\pi}u\sigma(x)} exp\left(-\frac{y^2}{2\sigma(x)^2}\right) + V_{bg}(x,y) \text{ (Eq. S1)}$$

$$\sigma(x) = \sqrt{\frac{2Kx^{\kappa}}{u}} \text{ (Eq. S2)}$$

Where Q is the emission rate, u is the wind speed, $H(x)$ is the Heaviside function, $\sigma(x)$ is the plume width across wind, and V_{bg} is the background column. K is the eddy diffusivity coefficient ($m^2\ s^{-1}$) and κ accounts for nonlinear spreading depending on the meteorological conditions. To obtain values for Q, K, V_{bg}, and κ, a least-squares method is used to minimize the cost function:

$$J(Q,K,V_{bg},\kappa) = ||V_{i,j} - G(x_i,y_i)||_2^2 \text{ (Eq. S3)}$$

Where $V_{i,j}$ is the observed NO_2 column density for a pixel with center (x_i,y_i). Given NO_2's short lifetime, it is necessary to multiply the Gaussian plume model by the decay term:

$$D(x,\tau) = H(x)exp\left(-\frac{x}{u\tau}\right) \text{ (Eq. S4)}$$

Where the lifetime, τ, is another fitting parameter. Since we are estimating emissions for a city source (Bangkok), the Gaussian model used in this context, accounts for fluxes increasing slowly across the source area. The city emissions are thus described by an emission map, p (x, y) and a decay term:

$$G_a(x,y) = G(x,y)\int_{-\infty}^{\infty} D(x',\tau)p(x-x',y)dx' \text{ (Eq. S5)}$$

The emission map can represent a two-dimensional Gaussian surface $p(x,y)$:

$$p(x,y) = \frac{1}{2\pi\sigma_x\sigma_y\sqrt{1-r^2}} \cdot exp\left(-\frac{(x-x_0)^2}{2\sigma^2{}_x(1-r^2)} - \frac{(y-y_0)^2}{2\sigma^2{}_y(1-r^2)} + \frac{r(x-x_0)(y-y_0)}{\sigma_x\sigma_y(1-r^2)}\right) \text{ (Eq. S6)}$$

S1.2 Integrated Mass Enhancement (IME) Inversion Method

Lastly, we estimate NO_2 emissions with the Integrated Mass Enhancement (IME) method, which relates the total mass of NO_2 observed within the detected plume to the underlying emission rate (Kuhlmann et al., 2024). This method is derived by integrating the Gaussian Plume model, $G(x,y)$, once the background, $V_{bg}(x,y)$ is subtracted over a singular polygon:

$$M = \int_{y_1}^{y_2}\int_{x_1}^{x_2} G(x,y) - V_{bg}(x,y)dx\,dy \text{ (Eq. S7)}$$

Where:

$$M = \int_{x_1}^{x_2} \frac{Q}{u} dx \text{ (Eq. S8)}$$

$$Q = \frac{u}{L}M \text{ (Eq. S9)}$$

Here, u is the effective wind speed, $L = x_2 - x_1$ is the plume length, Q is the emission rate, and M is the integrated total mass enhancement of the plume. M in practice is computed as:

$$M = \sum_{(i,j)\in\mathcal{P}_a}(V_{i,j} - V_{bg}) \cdot A_{i,j} \text{ (Eq. S10)}$$

Where $A_{i,j}$ is the pixel area and $\mathcal{P}_a$ is the integration area. For NO_2, a decaying gas, the decay term, $D(x)$, is included as well:

$$M = \int_{y_1}^{y_2}\int_{x_1}^{x_2} G(x,y) \cdot D(x)dx\,dy \text{ (Eq. S11)}$$

The final emission rate, Q, is determined as:

$$Q = \frac{1}{c}\frac{u}{L}M \text{ (Eq. S12)}$$

where c is a correction factor that corrects for decay along the plume direction:

$$c = \frac{u\tau}{L}\left(\exp\left(-\frac{x_1}{u\tau}\right) - \exp\left(-\frac{x_2}{u\tau}\right)\right) \text{ (Eq. S13)}$$

S2 Supplementary Figures

Table S1. Summary of WRF-Chem D01 validation statistics for Base (B), Updated (U), and bias-corrected (U+BC) simulations against independent observational datasets. Metrics include mean bias (MB), mean error (ME), normalized mean bias (NMB), normalized mean error (NME), root-mean-square error (RMSE), and Pearson correlation coefficient (CORR). Details of the evaluation methodology are provided in Sect. 6.

Dataset	Species	Model Run	MB	ME	NMB	NME	RMSE	CORR
GCAS	Tropospheric NO_2 column (molecules cm^{-2})	**B**	4.0E+15	5.5E+15	91.8	1.3E+2	8.9E+15	0.47
		U	-2.2E+14	2.1E+15	-5.0	49	3.1E+15	0.46
		U+BC	7.1 E+14	2.6 E+15	16	60.0	3.8 E+15	0.49
DC-8	NO_xO_3 NO_2 (ppbV)	**B**	0.27	0.53	17	33	1.2	0.94
		U	-1.0	1.0	-63	63	1.7	0.94
		U+BC	-0.77	0.77	-47	47	1.3	0.94
	CANOE NO_2 (ppbV)	**B**	0.3	0.57	20.0	36	1.3	0.94
		U	-1.0	1.0	-62	62	1.6	0.9
		U+BC	-0.73	0.74	-46	46	1.2	0.94

PCD Ground Monitors	NO_2 (ppbV)	**B**	6.9	8.2	73	87	11	0.45
		U	-4.6	4.9	-49	53	6.3	0.50
		U+BC	-2.4	3.9	-25	41	5.2	0.50
	NO_x (ppbV)	**B**	7.1	9.0	68	86	12	0.41
		U	-5.4	5.8	-51	55	7.8	0.57
		U+BC	-3.0	4.6	-28	44	6.7	0.53
	O_3 (ppbV)	**B**	5.2	11.4	17	37	16	0.86
		U	9.0	10.4	29	34	13	0.86
		U+BC	9.1	10.1	30.0	34	13	0.87
Pandora	Tropospheric NO_2 column (molecules cm^{-2})	**B**	4.5E+15	9.0E+15	31	62	1.1+16	-0.23
		U	-8.6E+15	8.6E+15	-59	59	1.1E+16	0.23
		U+BC	-6.4 E+15	6.5 E+15	-44	45	8.9 E+15	0.27

Table S2. Summary of WRF_{Base} wind validation statistics against surface observations (Thailand PCD) for 14 – 27 March 2024. Metrics include mean bias (MB), mean error (ME), root-mean-square error (RMSE), and Pearson correlation coefficient (CORR) included for wind speeds. ERA5 wind speeds align best with ground monitor observations in the BMR.

Dataset	**Species**	**Model Run**	**MB**	**ME**	**RMSE**	**CORR**
PCD Ground Monitors	Wind Speed ($m\ s^{-1}$)	WRF_{Base} D02	1.7	1.7	1.9	0.8
		WRF_{Base} D01	2.2	2.2	2.6	0.6
		ERA5	1.3	1.4	1.4	0.8
	Wind Direction (°)	WRF_{Base} D02	-13	19	24	-
		WRF_{Base} D01	7.2	23	32	-
		ERA5	-14	18	21	-

Table S3. Summary of WRF_{Base} PBLH statistics against airborne lidar observations (HSRL-2) for ASIA-AQ flight days, averaged over raster periods. Metrics include mean bias (MB), mean error (ME), normalized mean bias (NMB), normalized mean error (NME), root-mean-square error (RMSE), and Pearson correlation coefficient (CORR). Details of the evaluation methodology are provided in Sect. 6.

Date	MB	ME	NMB	NME	RMSE	CORR
18 March	190	420	28	62	590	0.53
19 March	-190	290	-31	48	340	0.27
21 March	330	510	43	67	650	0.31
23 March	150	410	21	56	480	0.54
25 March	190	450	27	63	550	0.72

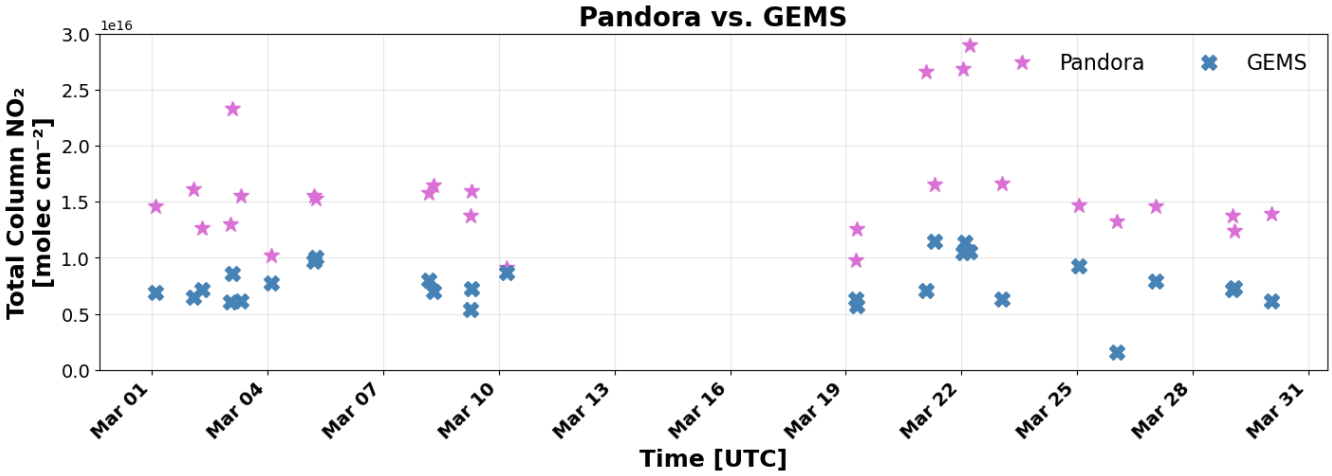

Figure S1. (a) Comparison of Pandora (pink) and GEMS (blue) total column NO_2 for high-quality observations during the March 2024. The ASIA-AQ deployment and model simulation period is representative of 14 – 27 March 2024. GEMS reproduces the temporal variability observed by Pandora (CORR = 0.7) but systematically underestimates column magnitudes (mean bias ≈ -9.2×10^{15} molecules cm^{-2}; mean ratio ≈ 0.6), with the largest discrepancies occurring during the stagnation event on 21 March 2024. GEMS is generally a factor of two lower than Pandora during this period.

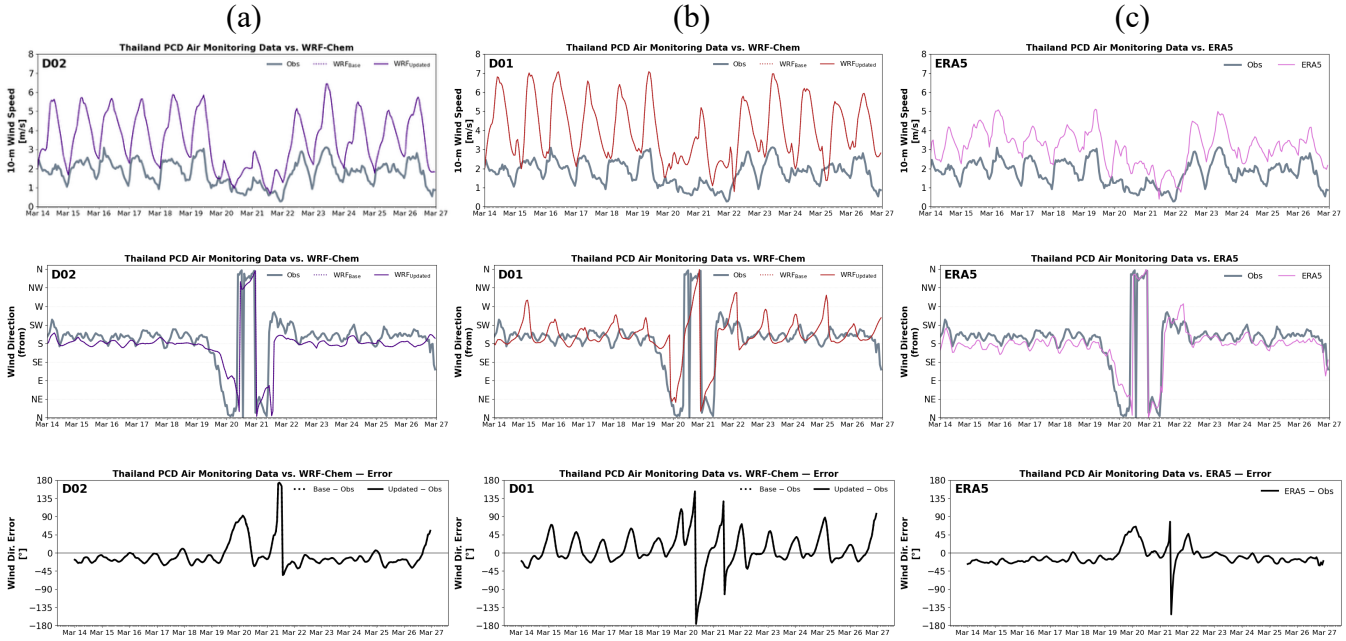

Figure S2. Comparison of (a) WRF_{Base} D02 (purple), (b) WRF_{Base} D01 (red), (c) ERA5 (pink) to Thailand Pollution Control Department (PCD) ground-monitor network (grey) wind speed (m s^{-1}), wind direction (from), and wind direction error during the ASIA-AQ deployment period (14–27 March 2024). Lines represent averages across stations within the BMR and surrounding regions. Both model domains and ERA5 overestimate wind speeds relative to surface observations, potentially due to unresolved urban canopy effects. These results suggest that improved urban parameterizations (e.g., a multi-layer urban canopy model) could enhance model performance. Error diagnostics also highlight misrepresentation of a short-lived northeasterly wind event on 20–21 March, leading to temporary errors in simulated transport direction.

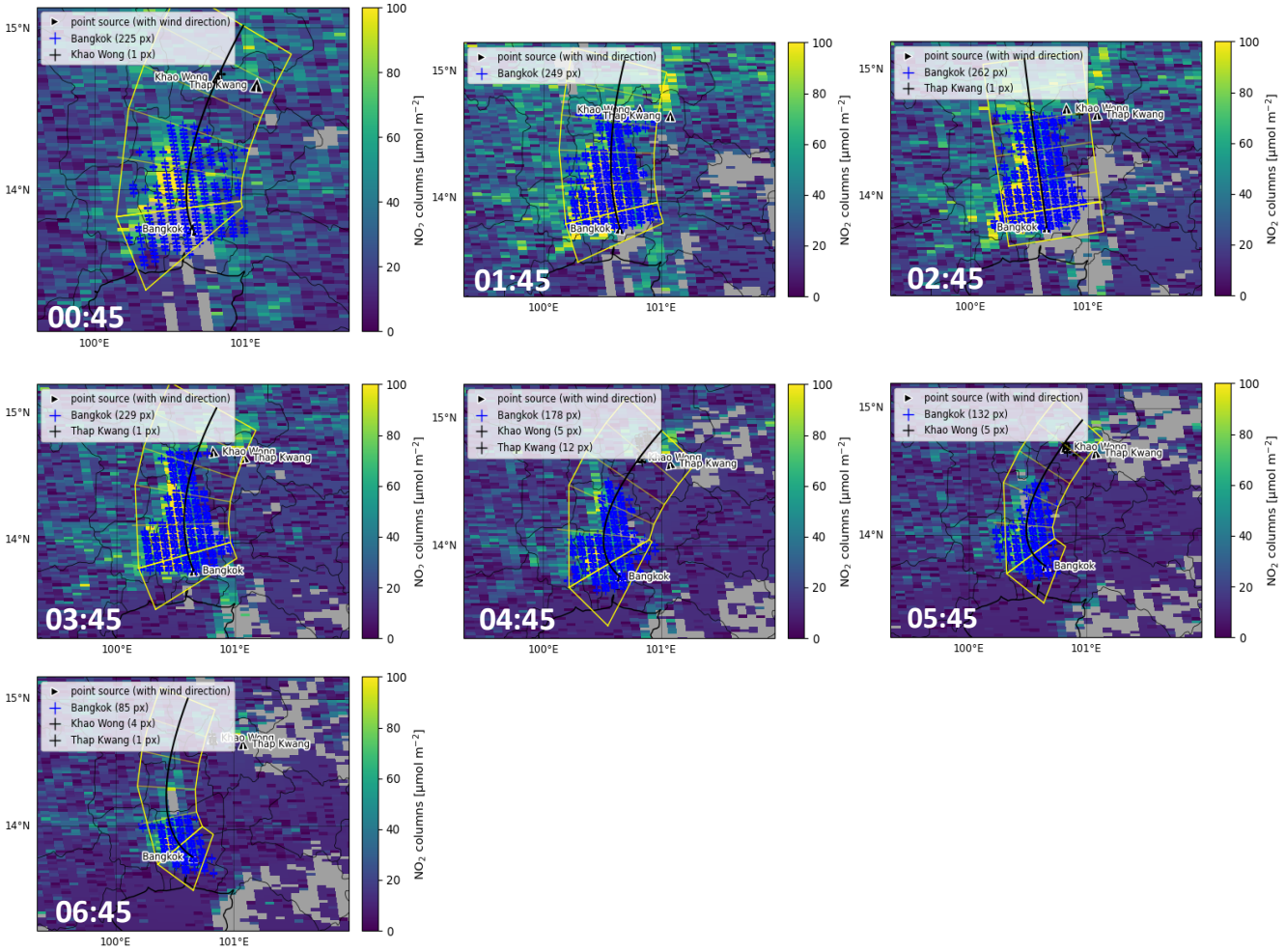

Figure S3. Example of the cross-sectional flux approach applied on 15 March 2024 using GEMS daytime measurements (00:45:00–06:45:00 UTC; 07:45:00–13:45:00 LT), generated with the *ddeq* Python package (Kuhlmann et al., 2024). Detected satellite pixels associated with the Bangkok urban plume are marked with blue ticks. A vector originating from Bangkok indicates the plume direction based on ERA5 wind fields at the source location. Khao Wong and Thap Kwang districts in Saraburi Province represent point sources distinct from the Bangkok urban plume, influenced by limestone quarry operations and heavy-truck transport (Makkhao and Prueksasit, 2023).

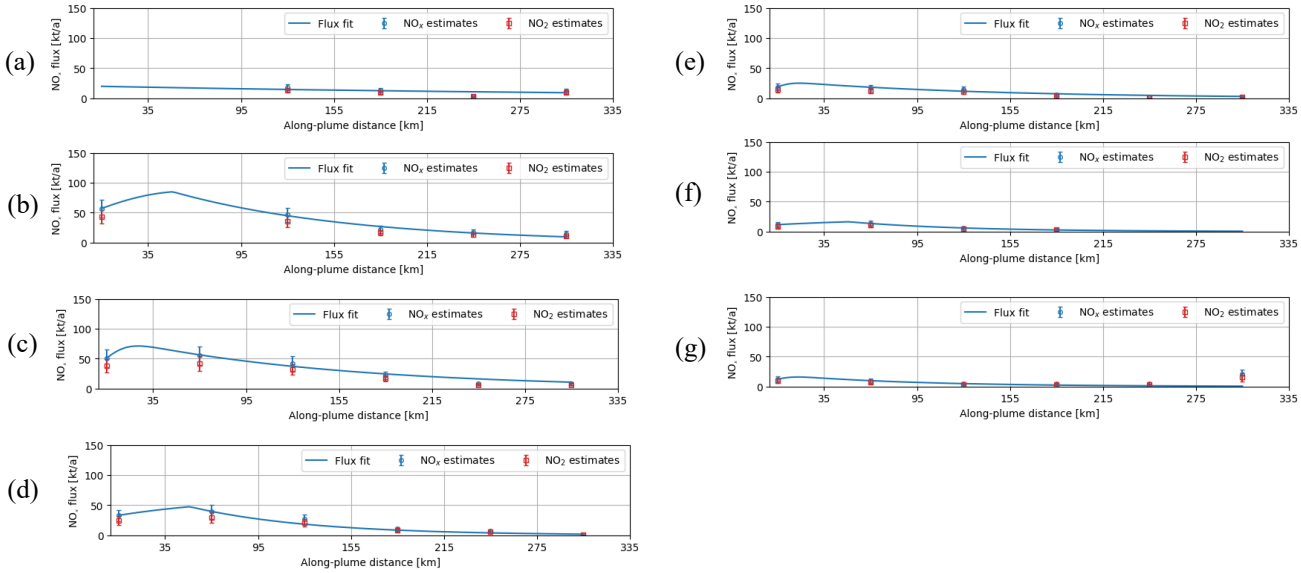

Figure S4. Examples of cross-sectional flux fits on 17 March 2024 for (a) 00:45:00 UTC (07:45:00 LT), (b) 01:45:00 UTC (08:45:00 LT), (c) 02:45:00 UTC (09:45:00 LT), (d) 03:45:00 UTC (10:45:00 LT), (e) 04:45:00 UTC (11:45:00 LT), (f) 05:45:00 UTC (12:45:00 LT), and (g) 06:45:00 UTC (13:45:00 LT), generated with the *ddeq* Python package (Kuhlmann et al., 2024). Derived NO_x fluxes vary throughout the daytime, with peak values in the morning hours and decreasing toward the afternoon, consistent with the daytime pattern of vehicular traffic emissions in the Bangkok Metropolitan Region (BMR).

(a)

(b)

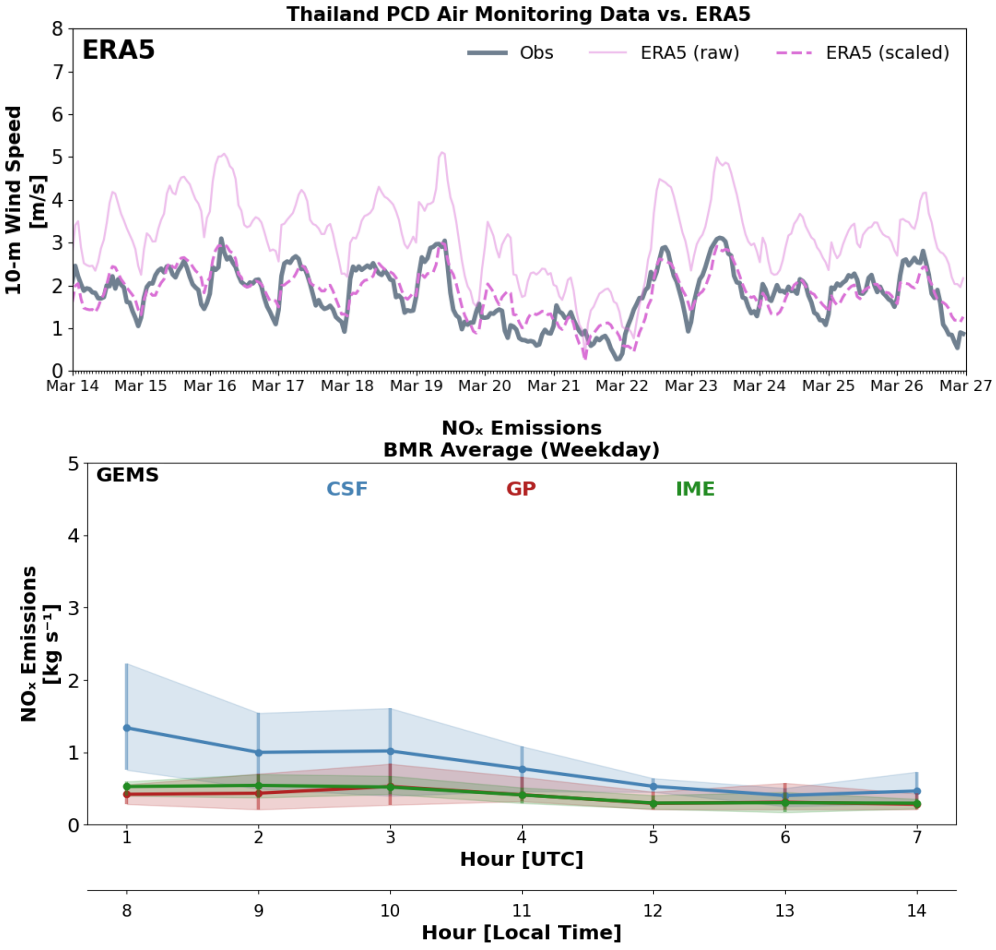

Figure S5. (a) ERA5 (solid pink) and Thailand Pollution Control Department (PCD) ground-monitor network (grey) wind speed (m s^{-1}) during the ASIA-AQ deployment period (14–27 March 2024). ERA5 wind speeds scaled by a factor of 0.6 are shown as dashed pink lines. (b) GEMS-derived daytime NO_x emissions (kg s^{-1}) estimated using the cross-sectional flux (blue), Gaussian plume inversion (red), and integrated mass enhancement (green) methods. Emissions represent averages across daytime hours and weekdays during the ASIA-AQ deployment. As a sensitivity test, ERA5 wind speeds were scaled by a factor of 0.6 prior to inversion to assess wind speed uncertainty. Reduced wind speeds lead to lower inferred emissions (≈40%), consistent with enhanced NO_2 accumulation under weaker transport and a reduced emission flux required to reproduce the observed columns. These adjusted emissions fall below those inferred from other observational constraints, suggesting that further wind speed reductions may not be appropriate for representing PBL-averaged transport in the BMR.

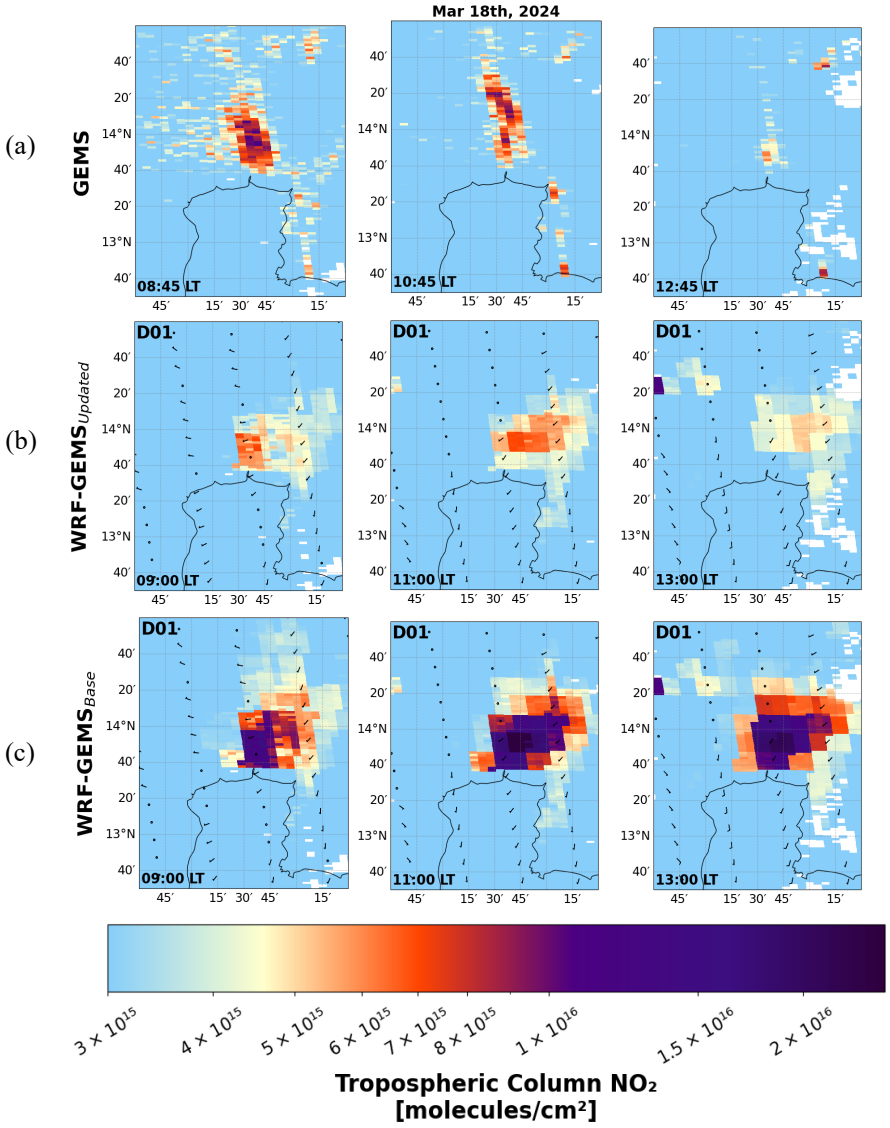

Figure S6. Spatial comparison over the BMR on 18 March 2024 of tropospheric NO_2 columns from (a) GEMS, (b) WRF-GEMS$_{Updated}$ D02, and (c) WRF-GEMS$_{Base}$ D02 for snapshots at 02:00:00, 04:00:00, and 07:00:00 UTC, corresponding to approximately 09:00:00, 11:00:00, and 14:00:00 LT.

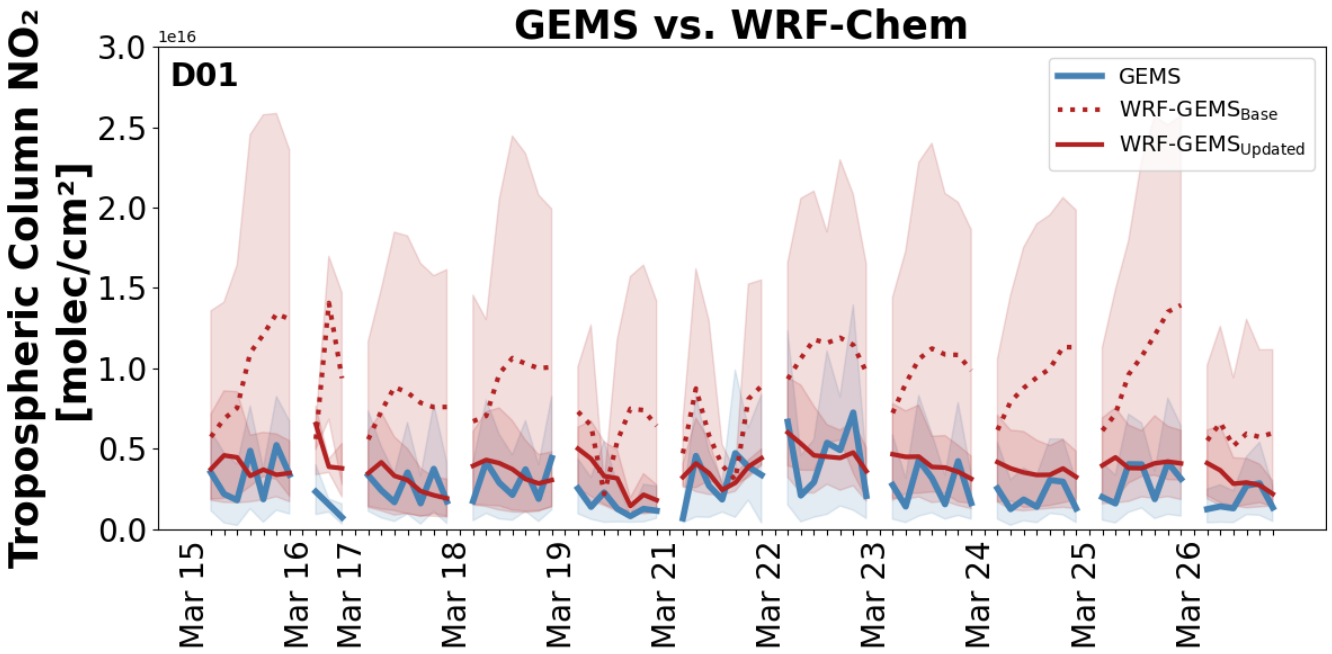

Figure S7. Daytime tropospheric NO_2 column comparison between GEMS (blue), WRF-$GEMS_{Base}$ D01 (dotted red), and WRF-$GEMS_{Updated}$ D02 (solid red) during the ASIA-AQ deployment period. Shaded regions indicate variability (10th–90th percentiles).

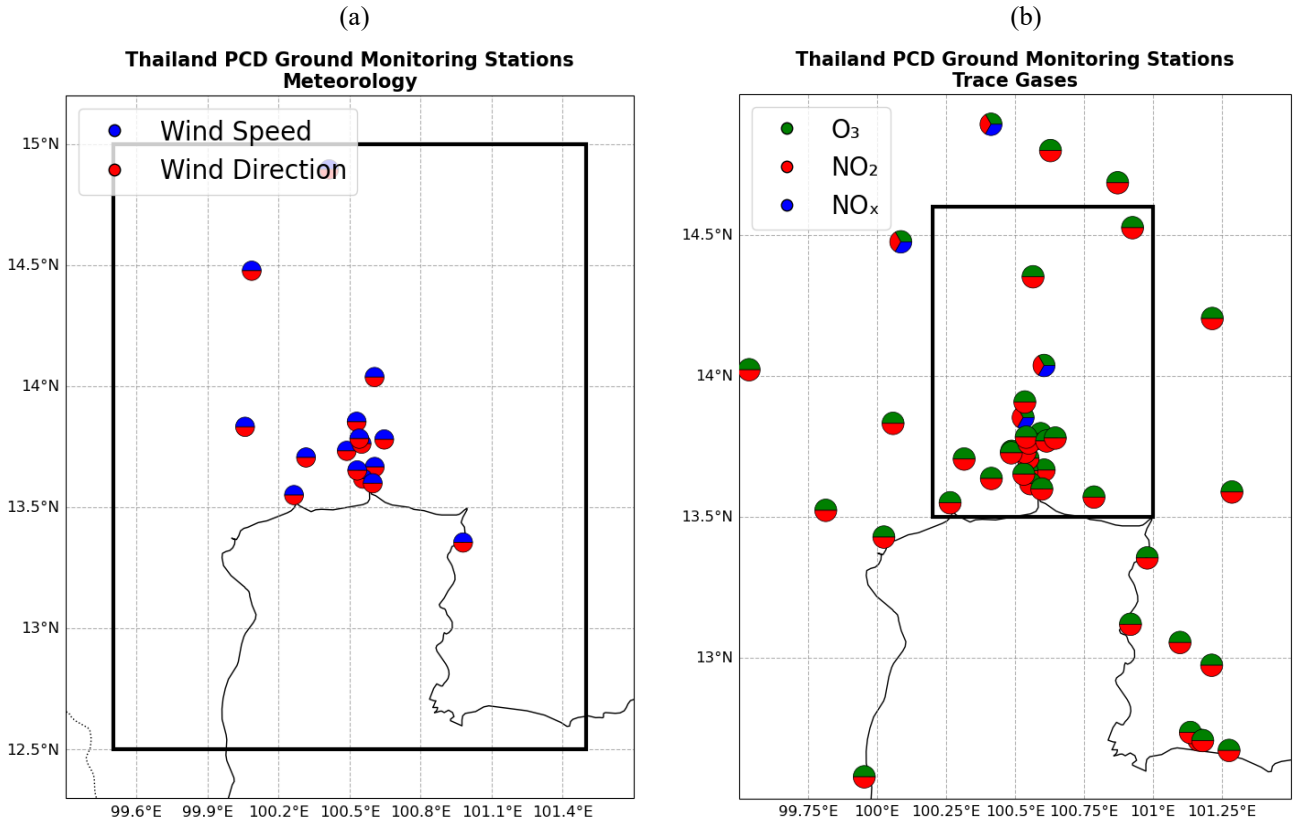

Figure S8. Locations of Thailand Pollution Control Department (PCD) ground-monitor stations used for evaluation of (a) meteorological variables (wind speed and direction) and (b) trace gases (NO_2, NO_x, O_3). Black boxes indicate stations included in the analysis. For trace gas evaluation, stations within the Bangkok urban plume were selected to assess the region where the inversion was applied, whereas meteorological evaluation includes a broader regional domain to better capture spatial variability in winds.

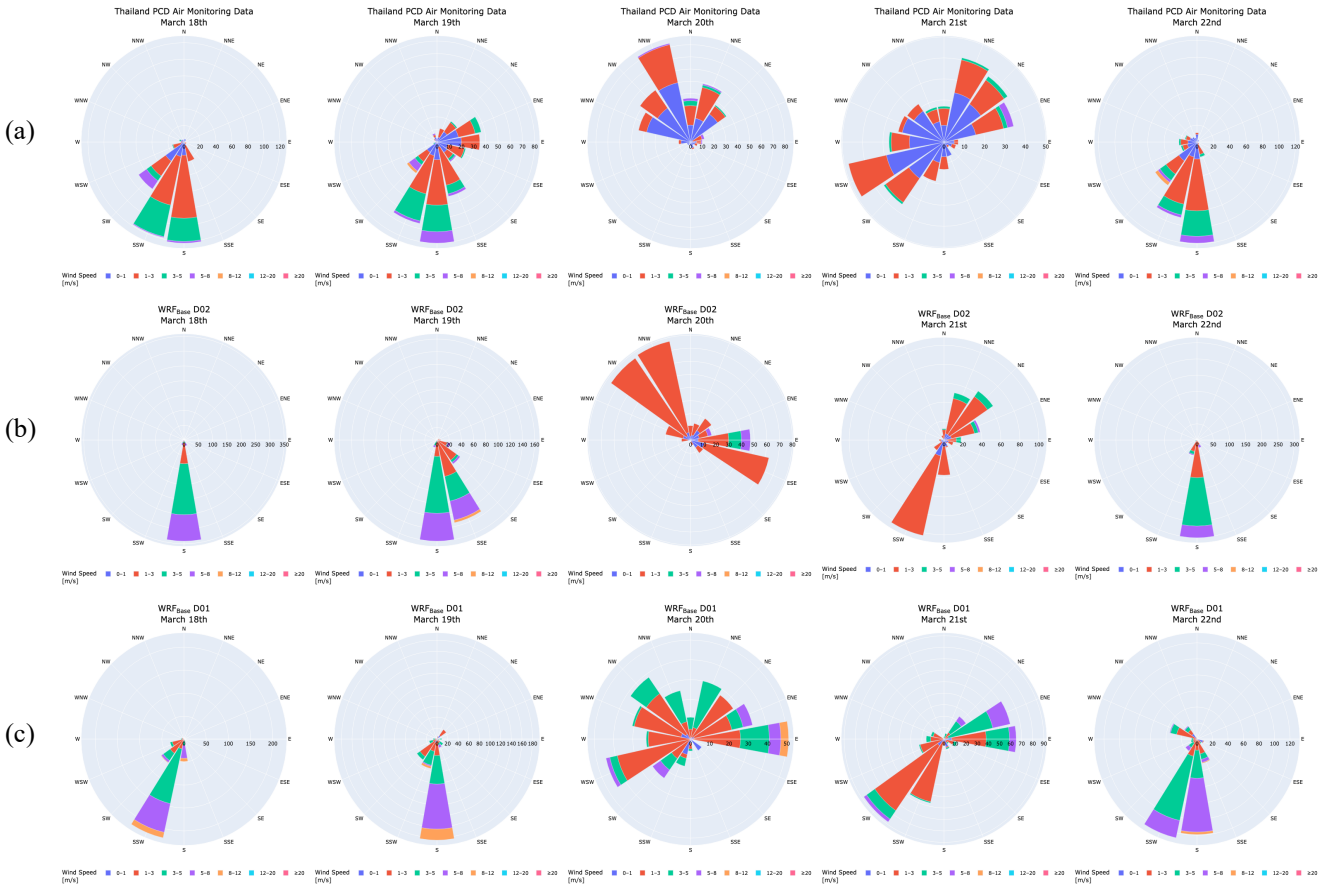

Figure S9. Comparison of observed wind roses (a) with modelled wind roses from (b) WRF_{Base} D02 and (c) WRF_{Base} D01 over the BMR for 18–22 March 2024. Panels show the frequency distribution of wind speed and direction. While the model captures the dominant southerly flow, wind speeds are consistently overpredicted in both domains. The largest discrepancies occur on 20–21 March, when the model fails to capture the observed shift toward northeasterly winds, likely contributing to transport and concentration errors during this period.

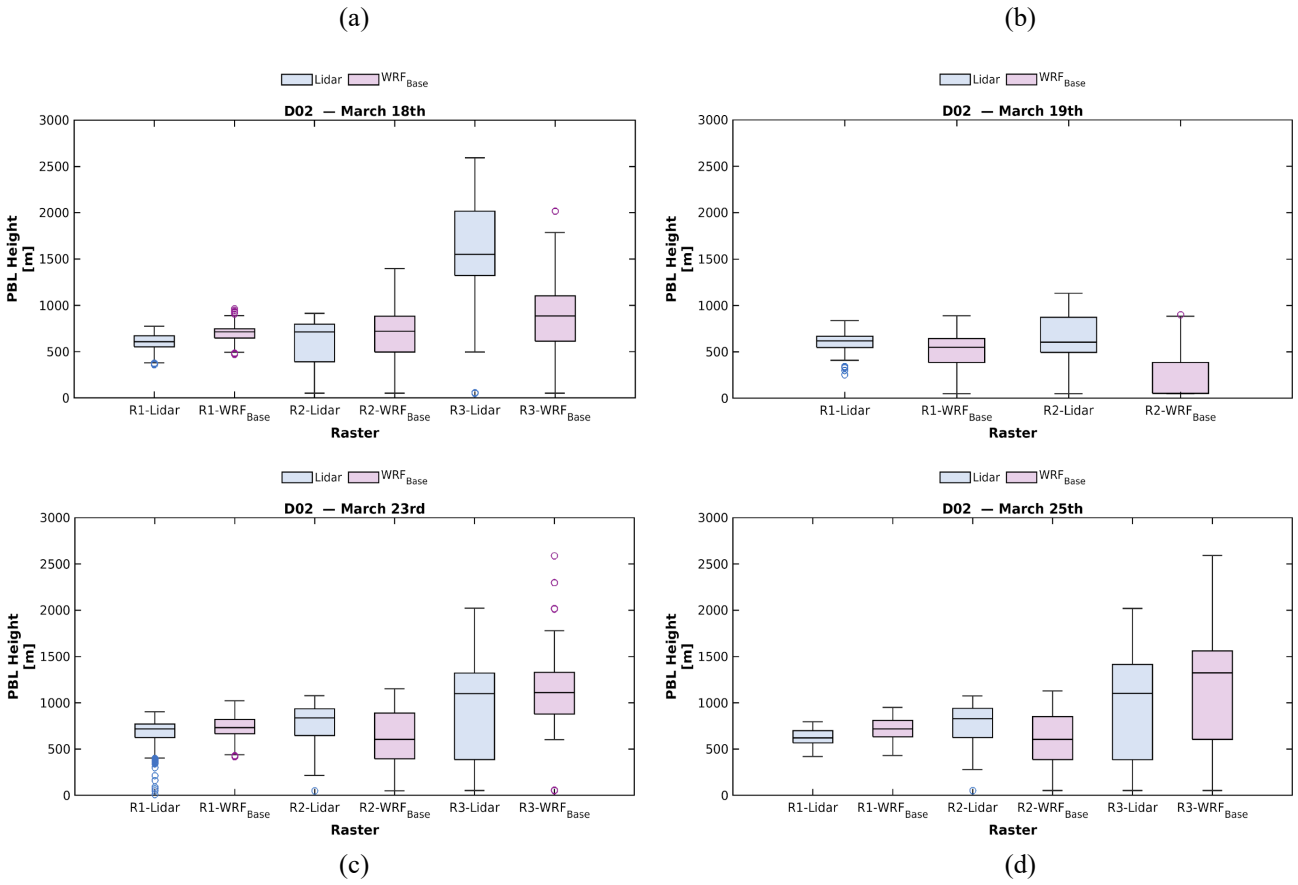

Figure S10. Evaluation of observed lidar-derived (blue) and modelled WRF_{Base} D02 (magenta) planetary boundary layer height (PBLH; m) for ASIA-AQ flight days on (a) 18 March, (b) 19 March, (c) 23 March, and (d) 25 March 2024. PBLH was derived from airborne HSRL-2 lidar observations following the methodology of Christopoulos et al. (2025). Overall, WRF-Chem reproduces the temporal evolution of the daytime boundary layer reasonably well on several days (CORR = 0.5–0.7), particularly during periods of strong convective mixing. However, the model exhibits biases in PBL depth. These results suggest that while WRF reasonably captures the timing of PBL evolution, it frequently misrepresents the magnitude of boundary layer development, particularly over-deepening the PBL during rapid daytime growth.

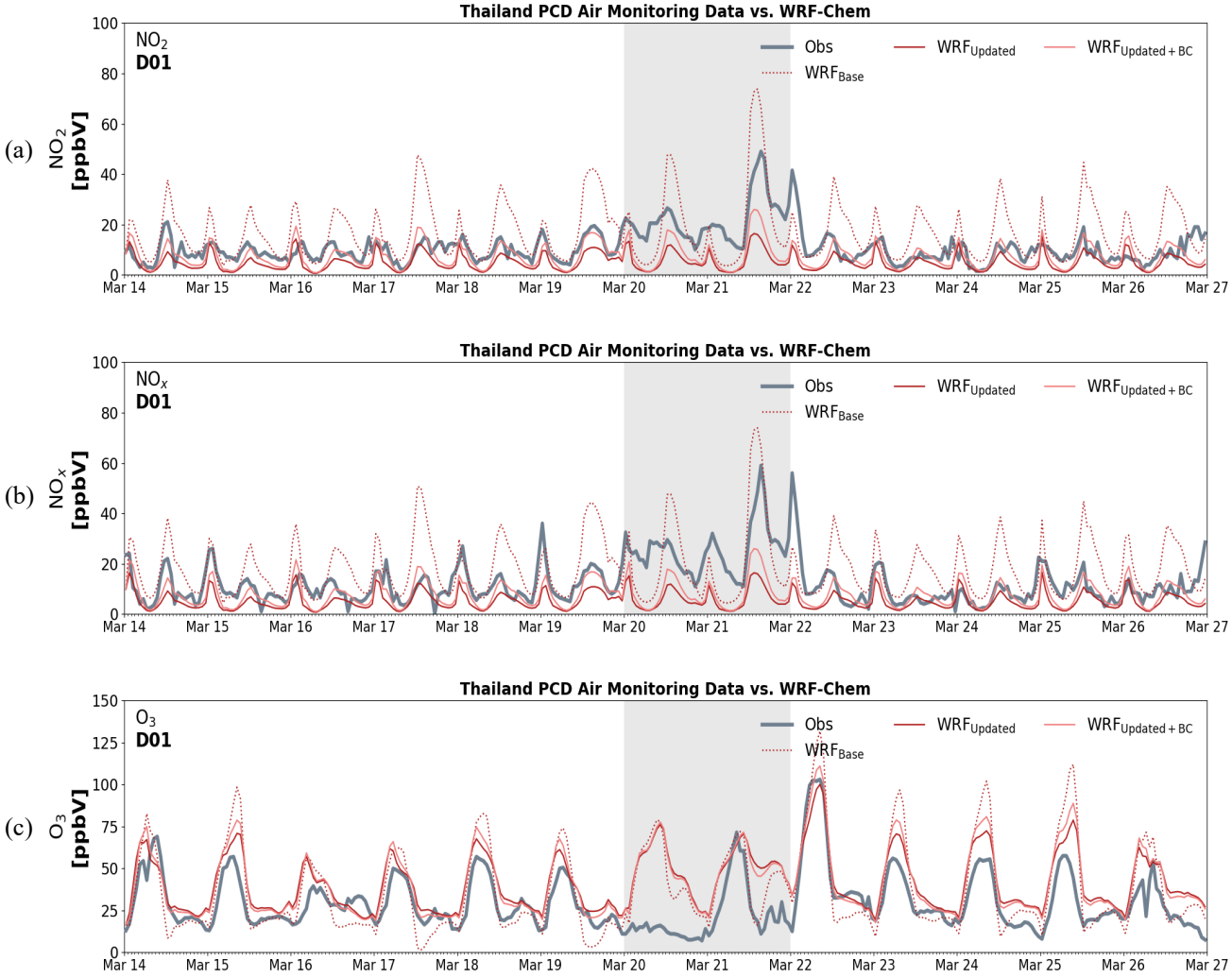

Figure S11. Comparison of WRF_{Base} D01 (dotted red),$WRF_{Updated}$ D01 (solid red), and $WRF_{Updated+BC}$ D01 (solid coral) simulations against Thailand Pollution Control Department (PCD) ground-monitor network observations for (a) NO_2 mixing ratio (ppbv), (b) NO_x mixing ratio (ppbv), and (c) O_3 mixing ratio (ppbv) during the ASIA-AQ deployment period (14–27 March 2024). Lines represent averages across stations within the Bangkok urban plume.

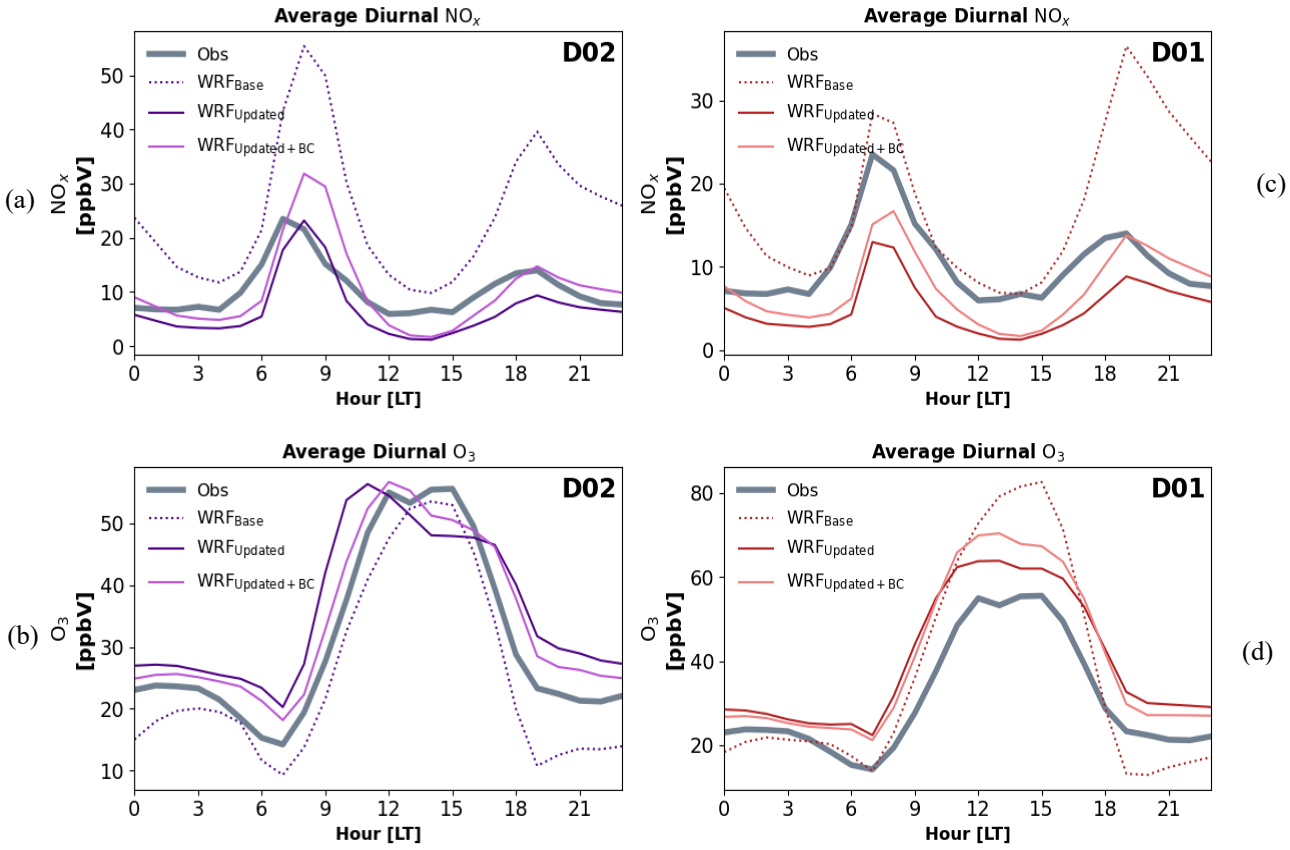

Figure S12. Average diurnal cycles of NO_x and O_3 for D02 (a,b) and D01 (c,d). Comparison of WRF_{Base} (dotted), $WRF_{Updated}$, and $WRF_{Updated+BC}$ simulations against Thailand Pollution Control Department (PCD) ground monitor network observations during the ASIA-AQ deployment period (14-27 March 2024).

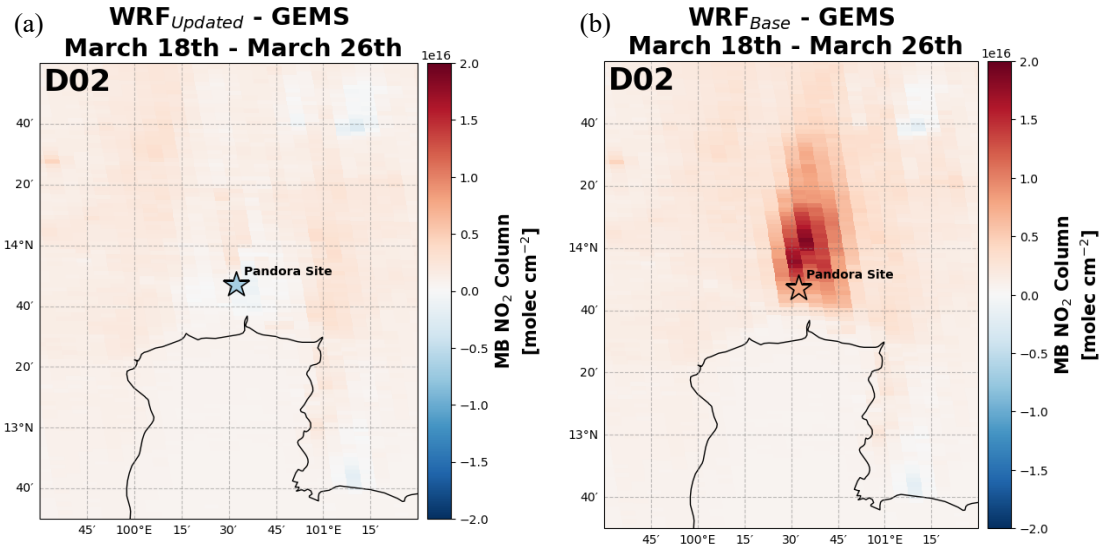

Figure S13. Spatial distribution of mean NO_2 column bias over the BMR averaged over 18–26 March 2024. Background shading represents WRF–GEMS bias, with the Pandora site location and corresponding model bias indicated. Results are shown for (a) $WRF_{Updated}$ and (b) WRF_{Base} simulations.

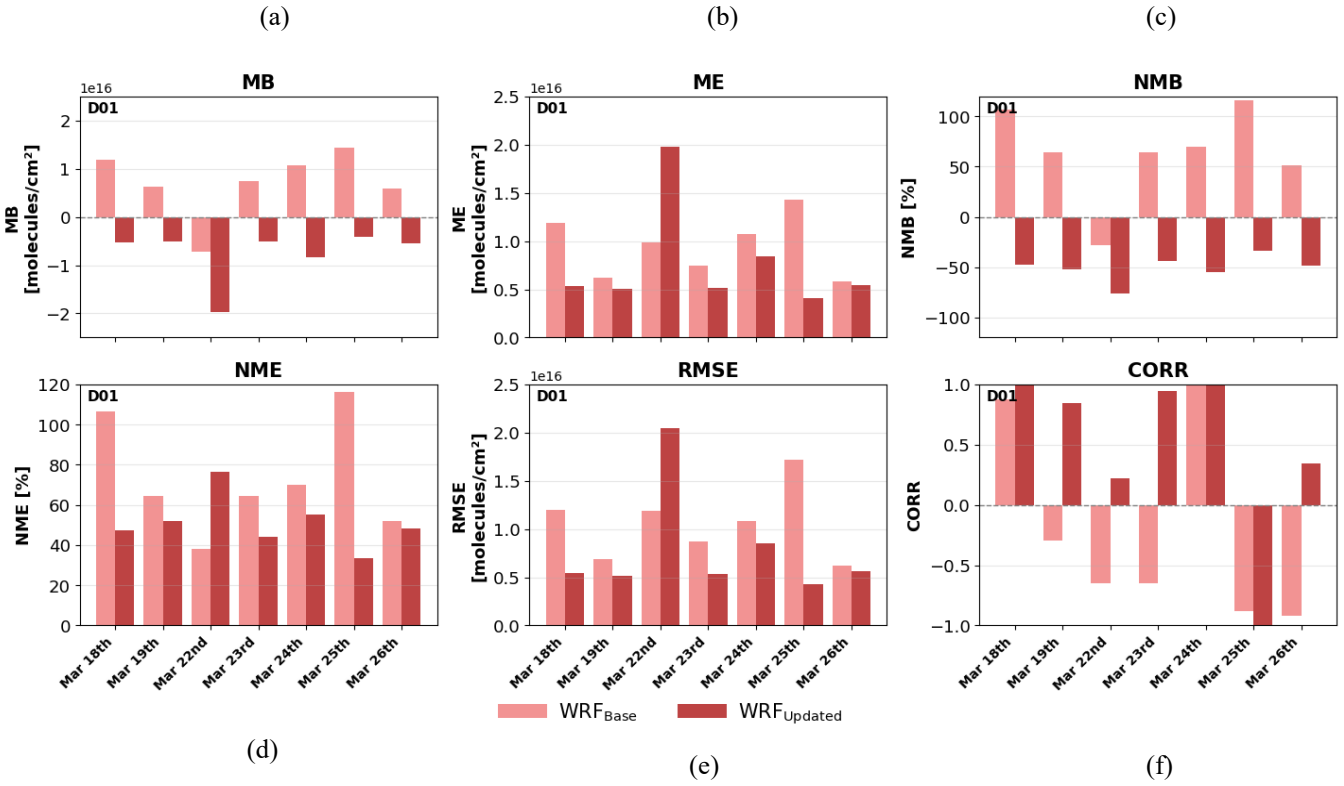

Figure S14. Statistical performance metrics for WRF_{Base} D01 (light red) and $WRF_{Updated}$ D01 (dark red) evaluated against Pandora observations during the ASIA-AQ deployment period (14–27 March 2024). Only days with high-quality Pandora data were included. Metrics include (a) mean bias (MB), (b) mean error (ME), (c) normalized mean bias (NMB), (d) normalized mean error (NME), (e) root-mean-square error (RMSE), and (f) correlation coefficient (CORR).

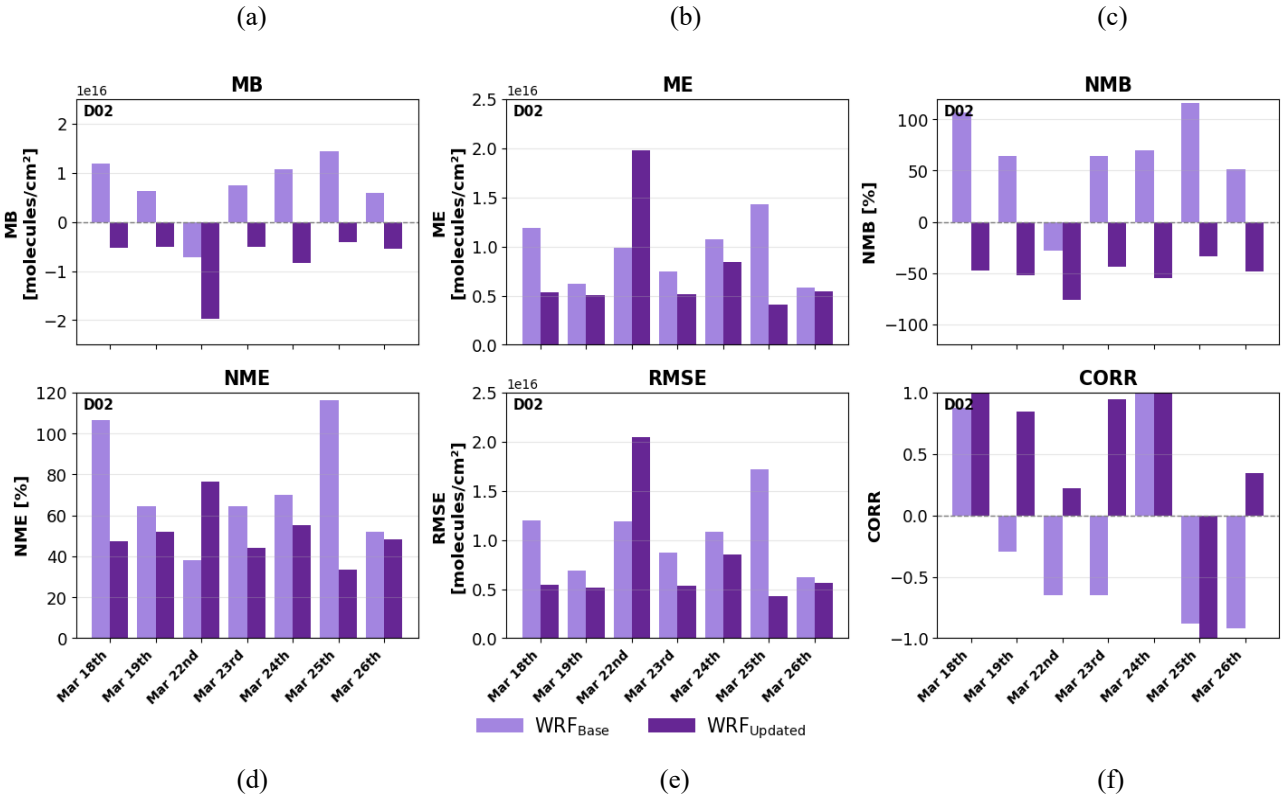

Figure S15. Same as Figure S14, but for WRF_{Base} D02 (light purple) and $WRF_{Updated}$ D02 (dark purple) evaluated against Pandora observations during the ASIA-AQ deployment period (14–27 March 2024).

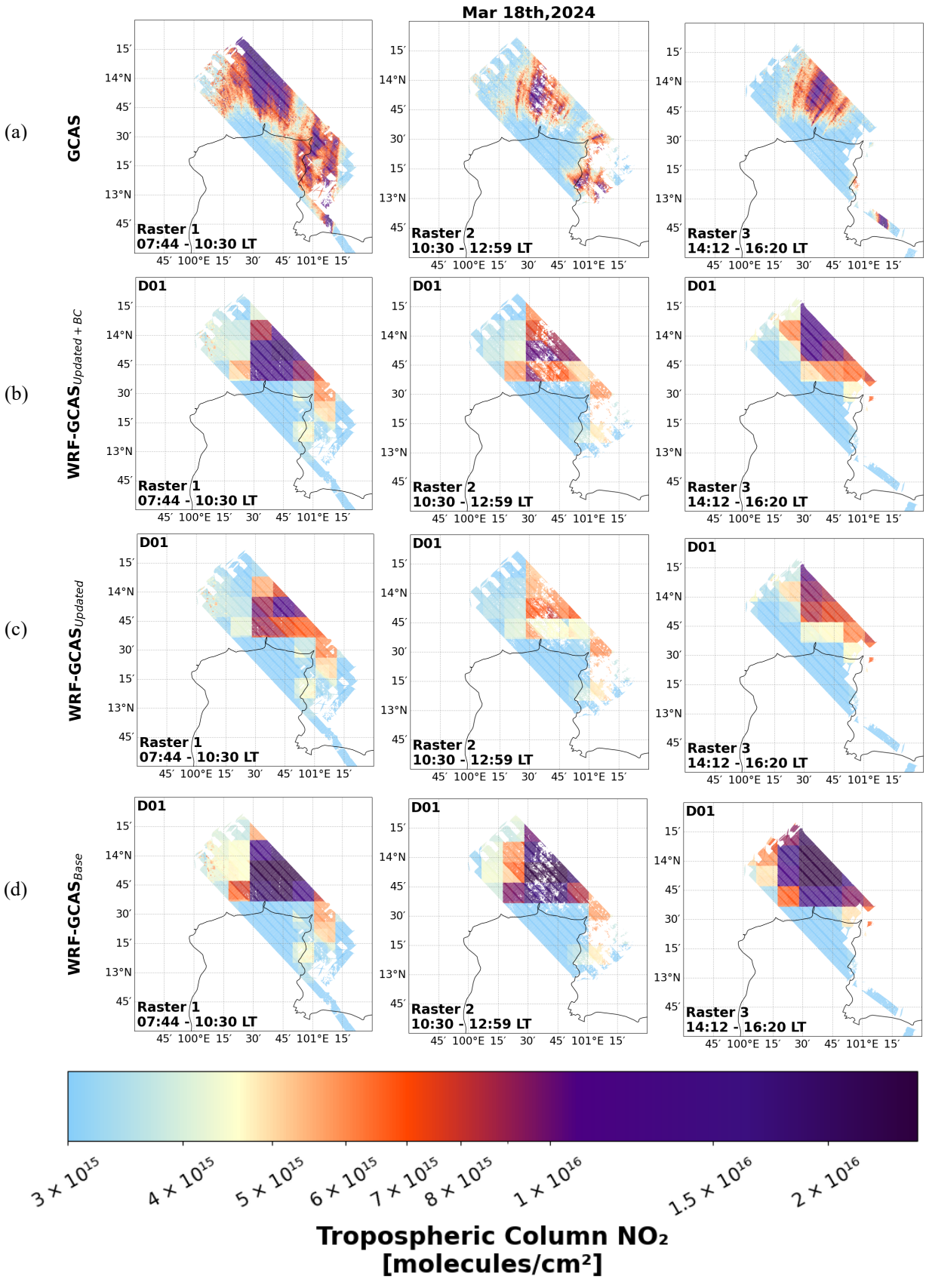
Mar 18th,2024
(a)
GCAS
(b)
WRF-GCAS Updated + BC
(c)
WRF-GCAS Updated
(d)
WRF-GCAS Base
D01
Raster 1
07:44 - 10:30 LT
Raster 2
10:30 - 12:59 LT
Raster 3
14:12 - 16:20 LT
15′
14°N
45′
30′
13°N
100°E 15′ 30′ 45′ 101°E 15′
3 x 10^15
4 x 10^15
5 x 10^15
6 x 10^15
7 x 10^15
8 x 10^15
1 x 10^16
1.5 x 10^16
2 x 10^16
Tropospheric Column NO₂
[molecules/cm²]

Figure S16. Spatial comparison over the BMR on 18 March 2024 of tropospheric NO_2 columns from (a) GCAS, (b) WRF-$GCAS_{Updated+BC}$ D01, (c) WRF-$GCAS_{Updated}$ D01, and (d) WRF-$GCAS_{Base}$ D01 for raster periods corresponding to morning, midday, and afternoon local time.

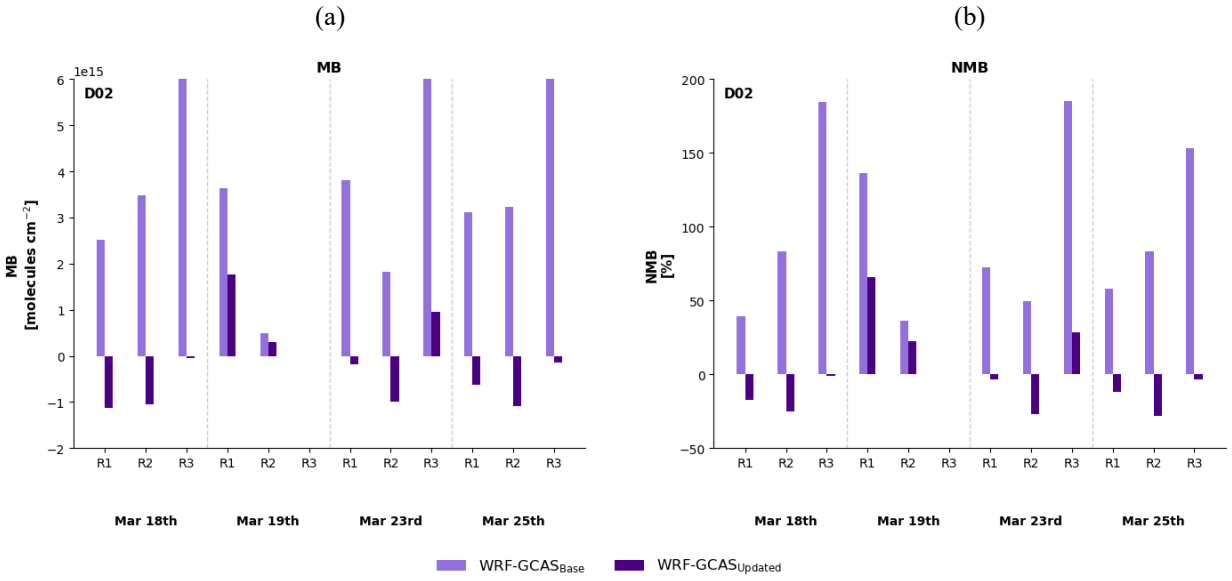

Figure S17. (a) Mean bias (MB) and (b) normalized mean bias (NMB) comparing WRF-$GCAS_{Base}$ D02 (light purple) and WRF-$GCAS_{Updated}$ D02 (dark purple) against GCAS observations for each raster period and ASIA-AQ flight day. Bias reductions in WRF-$GCAS_{Updated}$ D02 increase throughout the day, indicating improved representation of the daytime NO_2 evolution relative to the base simulation.

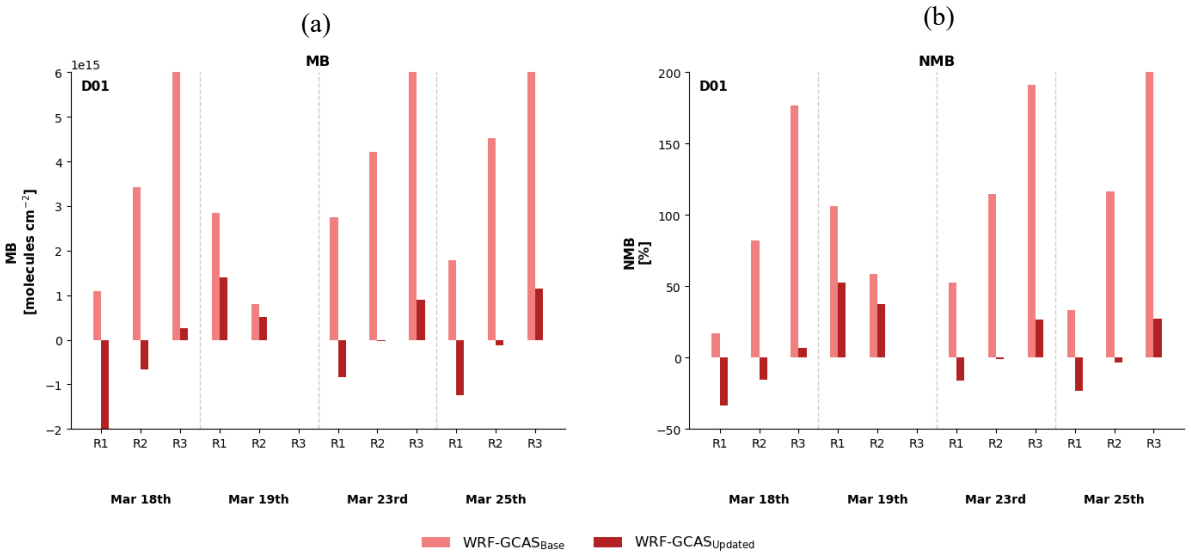

Figure S18. (a) Mean bias (MB) and (b) normalized mean bias (NMB) comparing WRF-GCAS$_{Base}$ D01 (light red) and WRF-GCAS$_{Updated}$ D01 (red) against GCAS observations for each raster period and ASIA-AQ flight day. Bias reductions in WRF-GCAS$_{Updated}$ D01 increase throughout the day, indicating improved representation of the daytime NO_2 evolution relative to the base simulation.

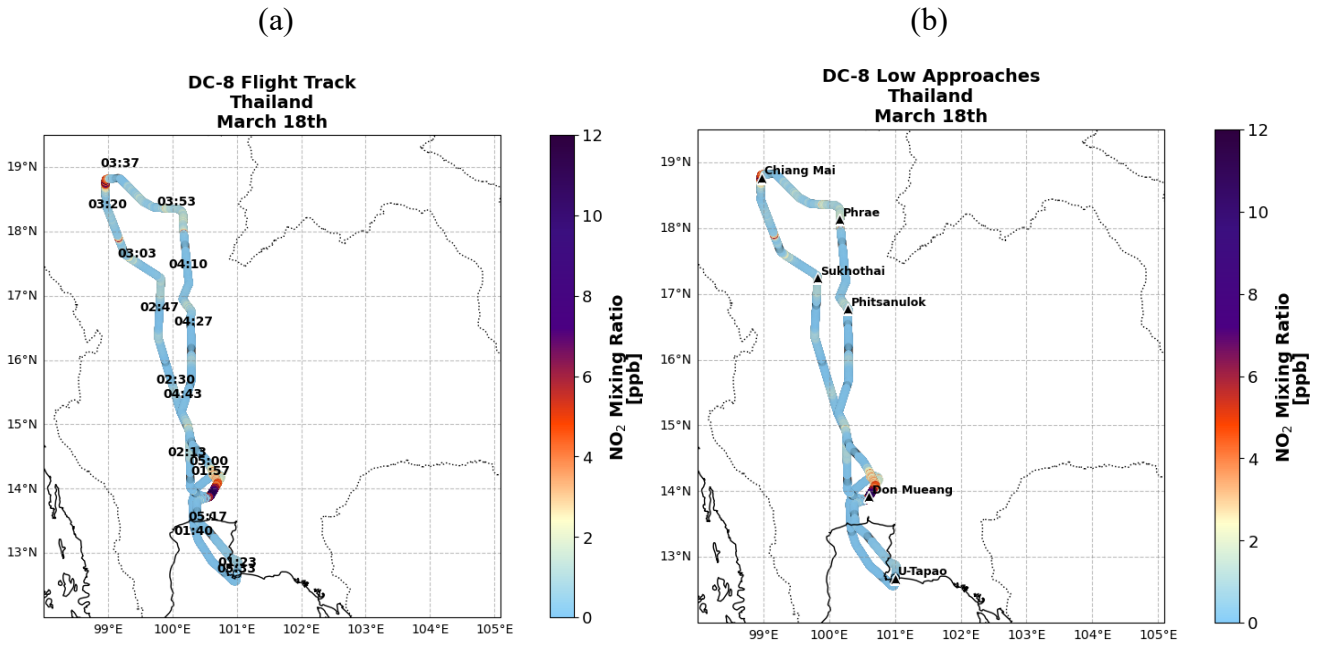

Figure S19. (a) Typical DC-8 flight track during the Thailand-led ASIA-AQ field campaign. The aircraft departed from U-Tapao Rayong Pattaya International Airport and flew northward across Bangkok and central Thailand toward Chiang Mai. (b) Locations of airports where the DC-8 conducted low approaches for profiling and sampling surface air quality (U-Tapao, Don Mueang, Phitsanulok, Sukhothai, Phrae, and Chiang Mai). NO_2 mixing ratios (ppbv) measured by NCAR's NO_xO_3 instrument are shown along the flight track, with time annotations indicated.

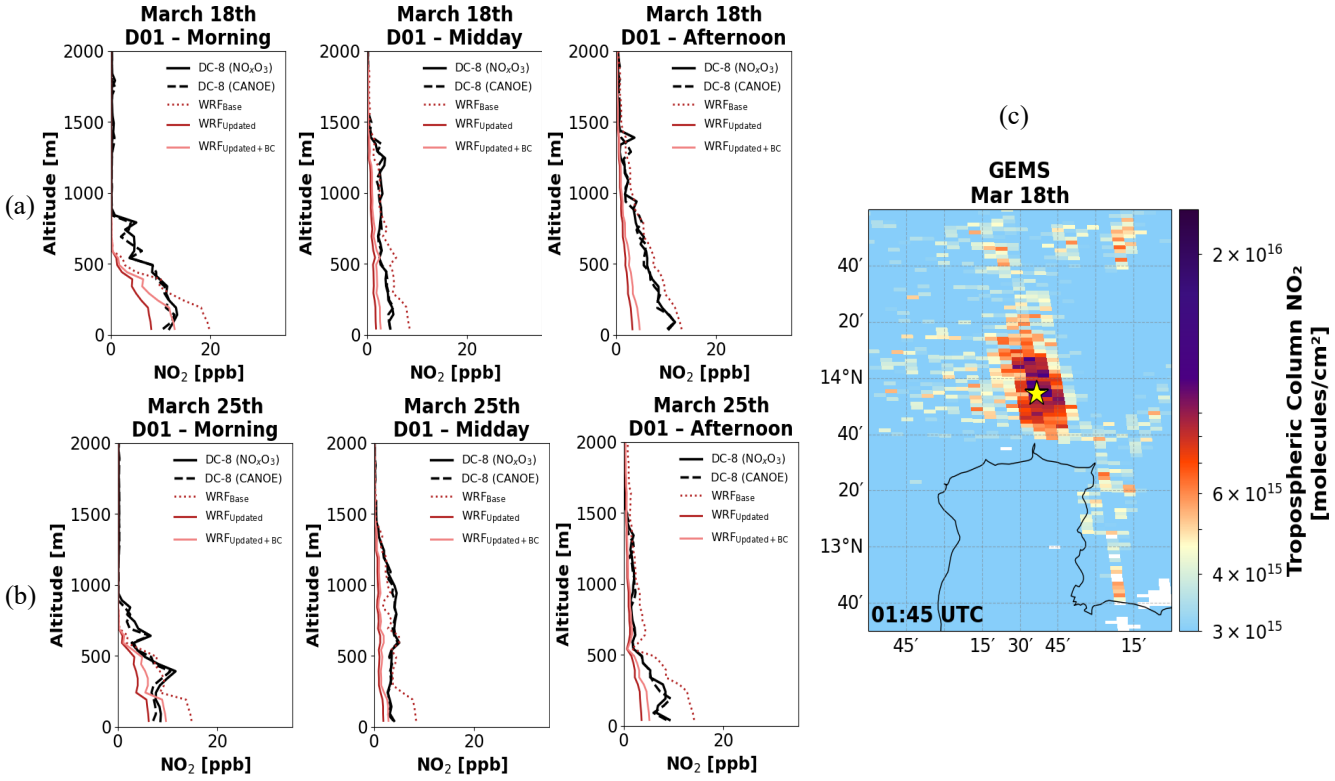

Figure S20. Comparison of WRF-Chem D01 simulations (WRF_{Base}: dotted red; $WRF_{Updated}$: solid red; $WRF_{Updated+BC}$: solid coral) with airborne in situ measurements from the CANOE (dashed black) and NO_xO_3 (solid black) instruments aboard the DC-8 for (a) 18 March and (b) 25 March 2024. Profiles are grouped by morning (06:00:00–11:00:00 LT), midday (11:00:00–13:00:00 LT), and afternoon (13:00:00–17:00:00 LT) approaches at Don Mueang International Airport, whose location relative to the Bangkok urban plume is shown in (c).

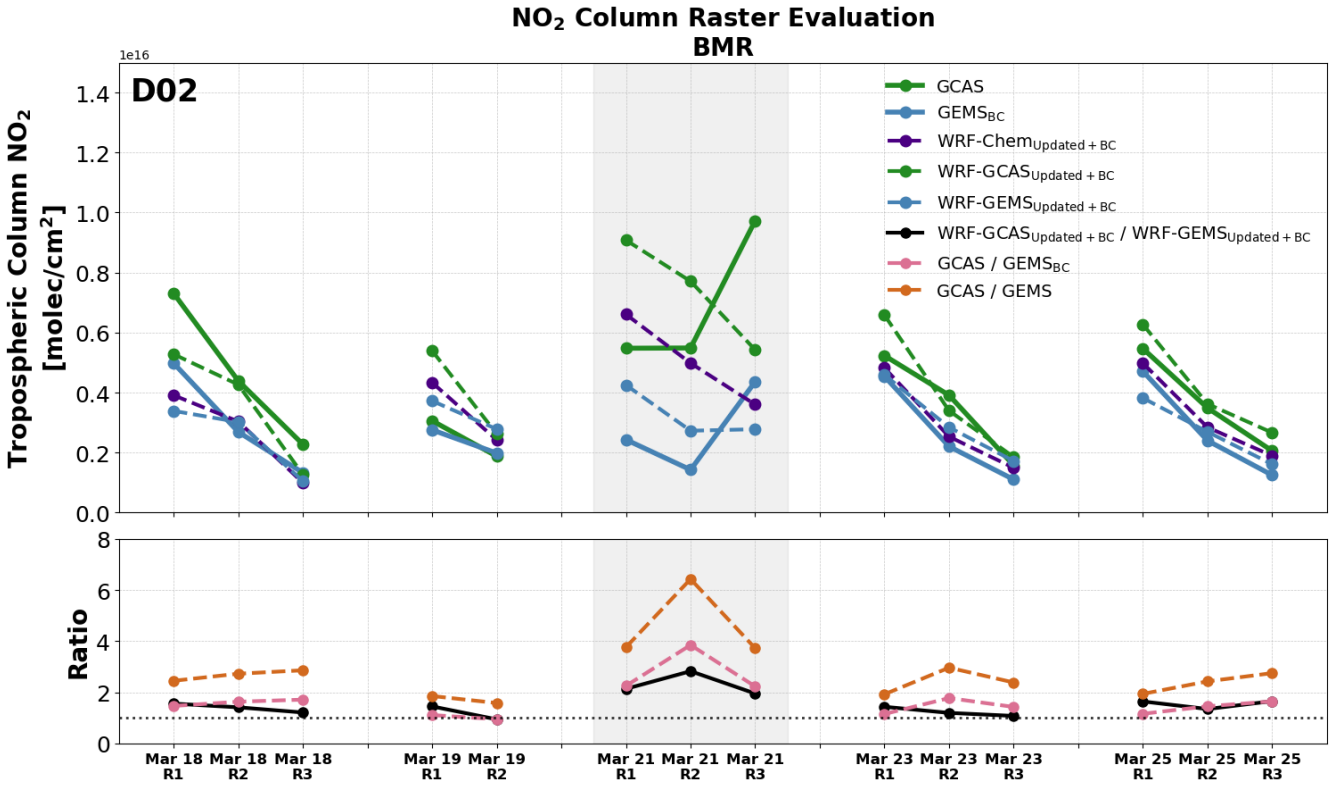

Figure S21. Daily raster comparison of tropospheric NO_2 columns from $WRF_{Updated+BC}$ D02 (dashed dark purple), $WRF\text{-}GCAS_{Updated+BC}$ D02 (dashed green), $WRF\text{-}GEMS_{Updated+BC}$ D01 (dashed blue), GCAS (green), and GEMS (blue) for ASIA-AQ flight days. Dashed model lines indicate simulations with instrument-specific averaging kernels applied. The difference in sensitivity between GCAS and GEMS measurements is illustrated by the ratio of WRF-GCAS to WRF-GEMS, plotted in black.